

## Quasiclassical Anderson transition and thermally activated percolative charge transport in single-crystalline ScN

Dheemahi Rao <sup>1,2</sup>, Debendra Prasad Panda <sup>1</sup>, Ashalatha Indiradevi Kamalasanan Pillai,<sup>3</sup> Akhil Tayal,<sup>4</sup> Magnus Garbrecht <sup>3</sup>, and Bivas Saha <sup>1,2,5,\*</sup>

<sup>1</sup>Chemistry and Physics of Materials Unit, Jawaharlal Nehru Centre for Advanced Scientific Research, Bangalore 560064, India

<sup>2</sup>International Centre for Materials Science, Jawaharlal Nehru Centre for Advanced Scientific Research, Bangalore 560064, India

<sup>3</sup>Sydney Microscopy and Microanalysis, The University of Sydney, Camperdown, New South Wales 2006, Australia

<sup>4</sup>Deutsches Elektronen-Synchrotron (DESY), 22607 Hamburg, Germany

<sup>5</sup>School of Advanced Materials (SAMat), Jawaharlal Nehru Centre for Advanced Scientific Research, Bangalore 560064, India



(Received 15 May 2023; revised 21 February 2024; accepted 1 April 2024; published 25 April 2024)

Quasiclassical Anderson transition (QAT) represents the crossover from metallic to activated conduction in heavily doped highly compensated semiconductors (HDHCSs) due to large-scale potential fluctuations. The spatial inhomogeneity of the charged dopants in HDHCSs localizes carriers, forming metallic droplets surrounded by potential barriers. Nitride semiconductors are seldom explored for HDHCS studies due to the difficulty in synthesizing stoichiometric high-quality films and self-compensation effects. Here we show conclusive experimental evidence of the QAT in compensated scandium nitride (ScN) single-crystalline films. Mg (hole) doping in *n*-type ScN increases the resistivity by nine orders and leads to semi-insulating films exhibiting a distinct crossover from the hopping conduction at low temperatures to thermally activated percolative transport at high temperature. The sign reversal of the Seebeck coefficient, anomalously low Hall mobility that increases with raising temperature, and persistent photoconductivity support the QAT and carrier transport mechanisms. QAT in single-crystalline nitrides could lead to lattice-matched devices with lasers, modulators, and dynamic holographic applications.

DOI: [10.1103/PhysRevB.109.155307](https://doi.org/10.1103/PhysRevB.109.155307)

### I. INTRODUCTION

Localization of elementary quasiparticles (electrons, photons, and phonons) in disordered and amorphous semiconductors is an intriguing phenomenon in solid-state physics [1–4]. The strength of localization strongly depends on the density of the disorder. At low disorder density, quantum self-interference of the quasiparticles leads to weak Anderson localization [5,6]. However, when the disorder density becomes large, strong localization results in a near absence of diffusion [7]. Parallel to the Anderson transition, heavily doped and highly compensated semiconductors (HDHCSs) can transition from metallic conduction at high doping to an activated transport at high compensation [8]. Such electronic transition stems from the potential fluctuations caused by the uncorrelated random distribution of charged dopants [8]. Unlike the conventional topological or compositional disorder, potential fluctuations are disorders in the form of random electric fields that can be treated quasiclassically [8,9]. Thus, the metal-insulator transition in HDHCSs represents a quasiclassical Anderson transition (QAT) that was originally formulated by Shklovskii and Efros [8]. Such an electronic transition in single-crystalline and epitaxial semiconductors could pave the way for their application in high-quality electronic and optoelectronic devices [10].

Fluctuating potentials in HDHCSs deform electronic bands, leading to spatially inhomogeneous electron distributions [8]. At a high doping level, the Fermi level lying above the fluctuation amplitude screens the potential fluctuations [Fig. 1(a-i)]. As the Fermi level lies in the conduction band ( $E_c$ ), electrons can easily move about in this equipotential surface under potential bias. However, with the increasing carrier compensation, the Fermi level is lowered into the band gap, and the potential fluctuation inhibits electronic transport. With the further lowering of the Fermi level, electrons are constrained only at the valleys that are separated in space [Fig. 1(a-ii)], thus forming carrier droplets [8,11]. The potential fluctuations now confine the carriers, and hence the resistivity increases. The amplitude of fluctuation increases with increasing compensation, and so does the resistivity. Thus, the metal-like heavily doped semiconductor becomes an insulator on heavy compensation.

The carriers in the droplets must hop (tunnel to adjacent droplets) unless activated to percolation level ( $\epsilon_p$ ), where they can undergo percolative transport. During percolation, the carriers move from the sides of the highest energy barriers, called the percolation barriers, without being obliged to climb those barriers [Fig. 1(a-ii)]. The conduction-band minima and the valence-band maxima in the reciprocal space [Fig. 1(b-i)] rumple, as shown in the zoomed Fig. 1(b-ii) of a small portion about the  $\Gamma$  point, where the bands can be considered almost flat. The fluctuation in the electronic bands with amplitude  $\gamma$  and radius  $R_s$  localizes the carriers in the valleys below

\*Corresponding author: bsaha@jncasr.ac.in; bivas.mat@gmail.com

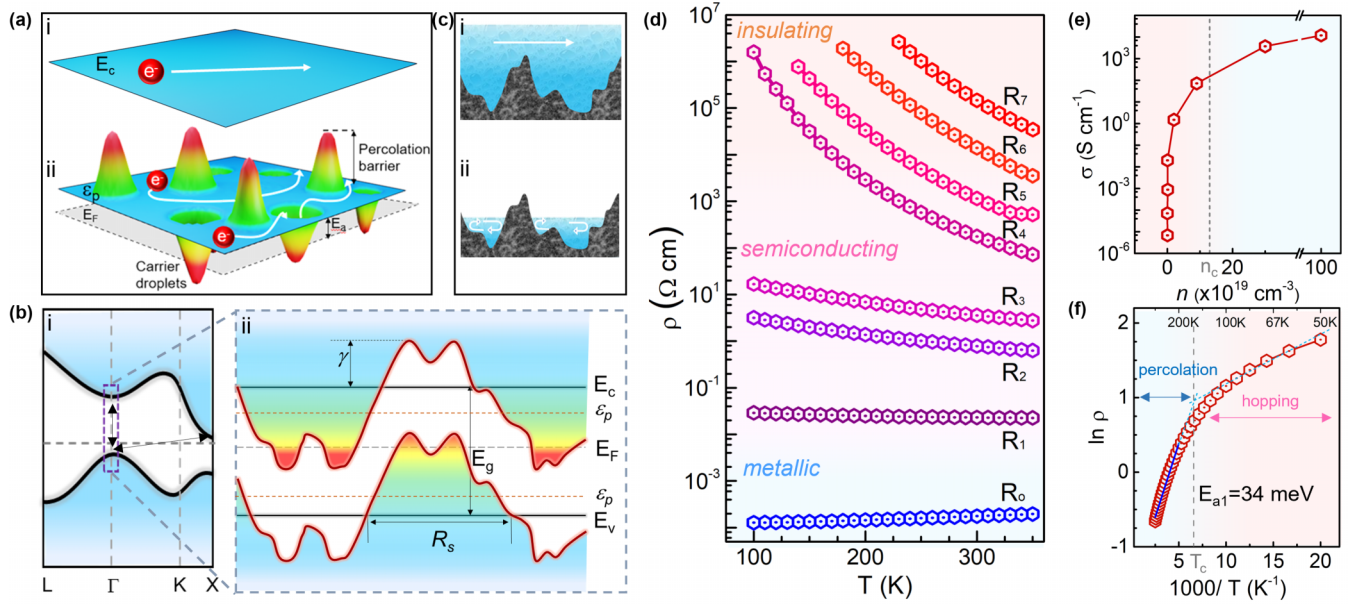


FIG. 1. (a) The schematic of (i) a flat conduction band modified into (ii) a surface with hills (barriers) and valleys (droplets) in an HDHCS. (b) The electronic bands showing (i) the direct and indirect band gaps and (ii) the potential fluctuations in a small region around the  $\Gamma$  point in an HDHCS, resulting in QAT. (c) Schematic diagram to describe the potential fluctuations in an HDHCS by drawing an analogy with water in a sea: (i) the underwater terrains are insignificant for the water flow when the water level is high; (ii) however, as the water level recedes, the water is constricted in the puddles, forming droplets. (d) Temperature-dependent resistivity of ScN with varying degree of compensation exhibiting more than nine orders of change in resistivity. (e) Changes in the room-temperature conductivity of ScN with decreasing electron concentration show a metal-insulator QAT beyond a critical  $n_c$ . (f) The crossover of hopping to activation-driven percolative transport with an activation energy of 34 meV for sample  $R_2$ .

$E_F$ , forming carrier droplets [8]. These potential fluctuations can be visualized like the terrains under the sea of electrons [Fig. 1(c)]. When the water level is much higher than the terrain height, water flows smoothly over the terrain [Fig. 1(c-i)]. The compensation of electrons is equivalent to lowering the water level that forms isolated water puddles in the deepest regions of the terrain [Fig. 1(c-ii)]. Note that, for low dopant concentrations, the impurities are uncorrelated. However, with increasing dopant concentration, Coulomb interactions among dopants could become substantial. In either of the cases, potential fluctuations and the metal-insulator transition (QAT) persist (see Sec. V in the Supplemental Material (SM) for more details [12]).

Though the theory of QAT metal-insulator transition in HDHCSs was proposed long ago, experimental verifications have been rare [8,13]. Signature of the QAT manifesting its influence on the electrical, optical, and photoemission properties in  $n$ -type Ge, Si, GaAs, GaN, and chalcopyrites [13–17] has been observed experimentally sporadically. However, a comprehensive demonstration of QAT metal-insulator transition and its impact on the physical properties of semiconductors is still missing.

Nitride materials show a wide spectrum of electronic properties with electrical conductivity ranging from  $10^5$ – $10^6$  S/cm in metals like TiN, ZrN, and HfN to  $\sim 10^{-12}$  S/cm in insulators such as AlN and h-BN [18,19]. Nitrides also have several widely acclaimed and industrially utilized semiconductors, such as GaN, InN, and InGaN, that show semiconducting transport properties [20,21]. Nitride materials, in general, exhibit several commendatory properties

such as high melting temperatures, high mechanical hardness, corrosion resistance, bright and shiny appearance for metallic nitrides, and possibilities of achieving high acoustic impedance [22,23]. However, for nitrides, along with the challenges in growing high-quality stoichiometric and epitaxial films, self-compensation effects further hinder achieving low carrier concentration and QAT [24]. Demonstration of QAT in nitride semiconductors would not only make them attractive for various electronic and optoelectronic devices with tunable resistivity, permittivity, and other physical properties, but it would also lead to potential device applications in lasers, optical modulators, photoconductors, and photorefractive dynamic holographic media [10].

Scandium nitride (ScN) is a unique material as it is the only stable III-nitride semiconductor exhibiting rocksalt crystal structure with an indirect band gap of 0.9 eV [23,25–28]. Its direct band gap is wider and is reported in the range 2.2–2.4 eV [29,30]. ScN exhibits a high thermoelectric power factor in the  $(2-4) \times 10^{-3} \text{ W m}^{-1} \text{ K}^{-1}$  range [31–35]. In addition to its use in thermoelectrics, ScN is also used as a buffer layer for development of low-dislocation-density GaN for LEDs and as a host for infrared polaritonics [36–38]. ScN thin films usually exhibit a high electron concentration in the  $10^{20}$ – $10^{21} \text{ cm}^{-3}$  range, which makes them highly degenerate semiconductors [39–44]. Persistent photoconductivity of ScN is also used to develop optoelectronic artificial synaptic devices exhibiting memory and learning [45]. Mg hole doping has been used successfully to develop  $p$ -type ScN films exhibiting a high hole concentration of  $\sim 2 \times 10^{20} \text{ cm}^{-3}$  at room temperature [46,47]. Unlike other nitride semiconductors such as GaN,

the substitutional oxygen and magnesium dopants in ScN do not introduce any defect states inside ScN's band gap, and the band edges remain unchanged [48]. Such a rigid-band electronic structure of ScN is extremely important as it allows for dopant inclusion and carrier compensation without self-compensation effects, which is a major challenge in other materials. In this work, we show QAT in emerging group-III(B) semiconducting scandium nitride single-crystalline thin films.

## II. THIN-FILM SAMPLE PREPARATION

The ScN thin films are deposited on 10 mm  $\times$  10 mm single-side polished MgO substrates inside a reactive DC magnetron sputtering in an ultrahigh-vacuum chamber with a base pressure of  $2 \times 10^{-9}$  Torr. The substrates are ultrasonicated in acetone and methanol for 10 min each and dried with nitrogen prior to loading into the ultrahigh-vacuum chamber. The substrates are heated to 800° and held there for 30 min for thermal desorption of the impurities and to achieve uniform heating before starting the deposition. Nitrogen and argon flow rates are set to 9:2 SCCM (where SCCM denotes cubic centimeter per minute at STP), and the chamber pressure is maintained at 5 mTorr. The DC power of Sc and Mg targets is varied from 100 to 125 W and from 6 to 15 W, respectively, to obtain different extents of compensation. Table 1 in the SM lists the electrical properties of the samples reported in this paper. Without any Mg doping, ScN exhibits an electron concentration, mobility, and resistivity of  $1.2 \times 10^{21}$  cm $^{-3}$ , 71 cm $^2$ /V s, and  $1.8 \times 10^{-4}$   $\Omega$  cm, respectively, at room temperature. Such a large  $n$ -type carrier concentration in ScN arises primarily due to the presence of oxygen as impurities and possible nitrogen vacancies [42,49]. Mg doping compensates  $n$ -type carriers and reduces the electron concentration. Since the activation energy of O<sub>N</sub> and Mg<sub>Sc</sub> are rather low, most dopants are electronically active and charged [50]. The structural, optical, and compositional characterizations of the thin films are presented in Sec. II of the SM (see also Refs. [51,52] therein).

## III. RESULTS AND DISCUSSION

### A. Electrical transport during QAT

The room-temperature resistivity of ScN films [Fig. 1(d)] increases by nine orders of magnitude with an increase in the Mg concentration from 0% ( $R_0$ ) to 2.6% ( $R_7$ ). At room temperature, the ScN film ( $R_0$ ) without any compensation exhibits a resistivity of  $1.8 \times 10^{-4}$   $\Omega$  cm, which is close to the resistivity of good metals [53]. The increasing resistivity with the increasing temperature suggests its degenerate semiconducting nature having a Fermi level in the conduction band. On adding Mg, the electrons are compensated, and the Fermi level moves down into the band gap to form a standard semiconductor in which resistivity decreases with increasing temperature. The amount of decrease in resistivity with increasing temperature becomes steeper for films with higher compensation ( $R_2$  to  $R_7$ ) that suggests an increase in their activation energy. The carriers need activation to overcome the potential barriers caused by the fluctuation. The ScN film with maximum compensation studied here ( $R_7$ ) has a resistivity

of  $1.5 \times 10^5$   $\Omega$  cm at room temperature, which is nine orders higher than that of  $R_0$ . The colossal increase in resistivity and the metallic-to-activated transport transition originate not only from the free movement of the Fermi level inside the band gap but also due to the localization of carriers by the potential fluctuations.

A plot of the resistivity ( $\rho$ ) vs electron concentration ( $n$ ) [Fig. 1(e)] shows the metal-insulator QAT vividly. The steep decrease in the conductivity occurs beyond the critical electron concentration ( $n_c$ ) of  $1 \times 10^{20}$  cm $^{-3}$ . This experimental critical concentration matches well with the theoretically calculated  $n_c$  of  $1.25 \times 10^{20}$  cm $^{-3}$  (where  $n_c = \beta N^{2/3}/a$  with constant  $\beta = 0.67$  and effective Bohr radius of impurity atom  $a = 1.6$  nm for ScN) [8]. The concept of minimum conductivity ( $\sigma_{\min}$ ) is proposed by Mott and is defined as  $\sigma_{\min} = c_3(e^2/h)N_m^{1/3}$ . With  $c_3 = 0.05$  and  $N_m = 2.5 \times 10^{20}$  cm $^{-3}$ ,  $\sigma_{\min}$  for ScN is 76.7 S/cm, which is in good agreement with the experimentally obtained value of  $\sim 78$  S/cm [Fig. 1(e)] (see details in Appendix A). During QAT, the conductivity falls sharply below  $\sigma_{\min}$  for  $n < n_c$  due to electron localization. A similar drop in conductivity was previously seen in Si [54]. For the samples  $R_4$  to  $R_7$  having electron concentration lower than  $n_c$ , it is difficult to even determine the carrier type. The sign of the Hall coefficient fluctuates, suggesting its ambipolar nature.

Another profound effect of potential fluctuation-driven QAT is the percolative charge transport [8]. The carrier transport undergoes a transition from the hopping to the thermally activated percolative kind at sufficiently high temperature marked as  $T_c$  in Fig. 1(f). The variation of resistivity  $\rho(T) = \rho_1 \exp(E_{a1}/kT) + \rho_2 \exp(E_{a2}/kT)^{1/2}$  has two regimes across  $T_c$ . The Arrhenius fit to the linear regime at temperatures higher than  $T_c$  yields the activation energy required to excite the carrier from the droplet in the valley to the percolation level ( $E_{a1} = |E_F - \varepsilon_p|$ ). A representative  $\ln \rho$  vs  $1/T$  plot for sample  $R_2$  that is at the onset of localization exhibits a percolation activation energy of 34 meV [Fig. 1(f)]. The activation energy can be as high as  $E_g/2$ , which is 450 meV for ScN. Below  $T_c$ , electrons exhibit Efros-Shklovskii (ES) variable range hopping (VRH), having a function from  $\rho(\rho) = \rho_0 \exp(E_{a2}/kT)^{1/2}$ . The fitting also reveals an activation energy of 16 meV for the hopping conduction at low temperatures (see Appendix B).

The activation energy ( $E_{a1}$ ) and the critical temperature ( $T_c$ ) corresponding to the percolative transport increase with an increase in the compensation [Fig. 2(a)]. This observation complies with the fact that the amplitude of the potential fluctuation that contains the electron droplets increases at higher compensation levels. The radius of the droplet and the amplitude of the potential fluctuation are calculated, and they increase from 1 nm and 13 meV for  $R_2$  to 550 nm and 790 meV for  $R_7$ , respectively (see details in Appendix B). Anomalously low Hall mobility is yet another signature of HDHCSs. The compensated ScN have more than ten times lower mobility at room temperature than the uncompensated heavily  $n$ -type ScN. Since the carriers in HDHCSs are localized in the droplets, the definition of mobility in itself does not have the same meaning as in the case of uniform potential. The variation of mobility with temperature for sample  $R_4$  is

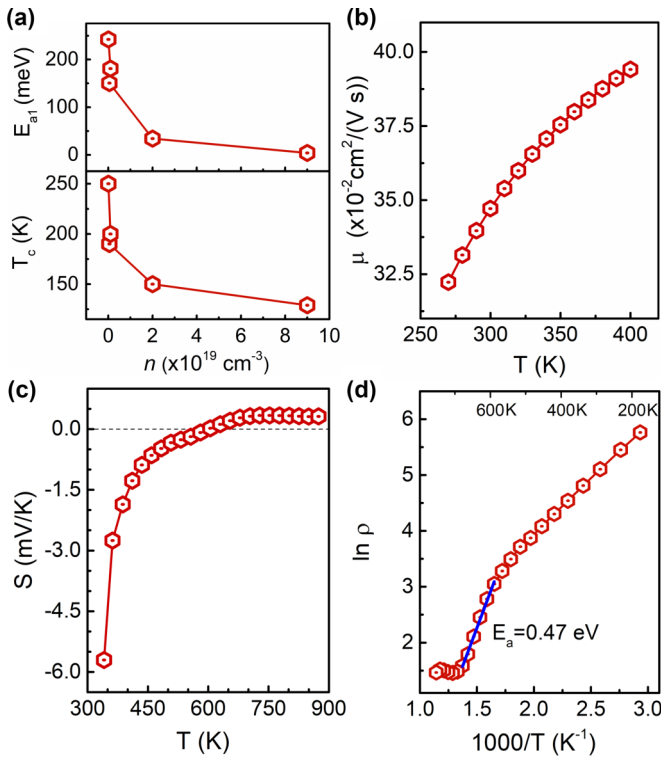


FIG. 2. (a) Variation of activation energy ( $E_{a1}$ ) and critical temperature ( $T_c$ ) corresponding to the percolative transport increases with increasing compensation for samples  $R_1$ ,  $R_2$ ,  $R_4$ ,  $R_5$ , and  $R_6$ . (b) The mobility of  $R_4$  increases at higher temperatures due to increased screening of the potential barriers. (c) The Seebeck-coefficient ( $S$ ) for a compensated ScN  $R_4$  changes sign from negative to positive at  $\sim 600$  K, indicating the bipolar nature. (d) The temperature-dependent resistivity of  $R_4$  shows an activation of 0.47 eV at  $\sim 600$  K, at which the sign of the Seebeck coefficient flips.

presented in Fig. 2(b). Generally, the mobility decreases at higher temperatures due to enhanced phonon scattering [46]. On the contrary, in HDHCSs, the carrier mobility increases at higher temperatures due to the screening of the potential

fluctuation barriers [8,55,56]. The variation of Seebeck coefficient ( $S$ ) in the 300–850 K range for sample  $R_4$  is shown in Fig. 2(c), which changes from negative to positive at  $\sim 600$  K, suggesting the switching of the majority carrier type. Such a behavior arises as the activation energies of electrons and holes become nearly equal in the HDHCS. At about the same temperature, the electrical resistivity also has an activation [Fig. 2(d)] of 0.47 eV that can be attributed to the activation of the holes to its percolation level that will result in a positive Seebeck coefficient.

### B. Persistent photoconductivity in HDHCSs

Persistent photoconductivity (PPC) is one of the pronounced signatures of the existence of potential fluctuations [57,58]. The room-temperature photoresponse of a compensated ScN sample  $R_4$  is shown in Fig. 3(a). The sample is illuminated with white light for 1 h, and the variation in current is measured at a constant bias of 1 V in a vacuum chamber. On illumination, compensated ScN exhibits positive photoconductivity, where the current increases. When the light is turned off, the current initially drops rapidly by  $\sim 35\%$  in 10 min. Thereafter, the decay slows down significantly such that it takes several hours to return to its initial dark state. The persistence in the photocurrent lasts for several minutes to several days, depending on the extent of compensation. Such long-lasting persistence in photoconductivity (frozen photocurrent) occurs as the photogenerated electrons and holes rapidly move in opposite directions and are localized (trapped) by the potential barriers at different regions in space, inhibiting their recombination. The PPC decay in compensated ScN is fitted with three exponential functions. The first two time constants,  $\tau_1$  ( $\sim$ tens of seconds) and  $\tau_2$  ( $\sim$ hundreds of seconds) increase with increasing temperatures because of the electron redistribution at the percolation sites. The third time constant ( $\tau_3$ ) is in the range of  $10^5$  s and is the pivotal component of PPC [Fig. 3(b)]. Such large time constants result from the carrier localization by the fluctuating potential barriers. As the temperature increases, the hopping probability increases, effective barrier height decreases, and

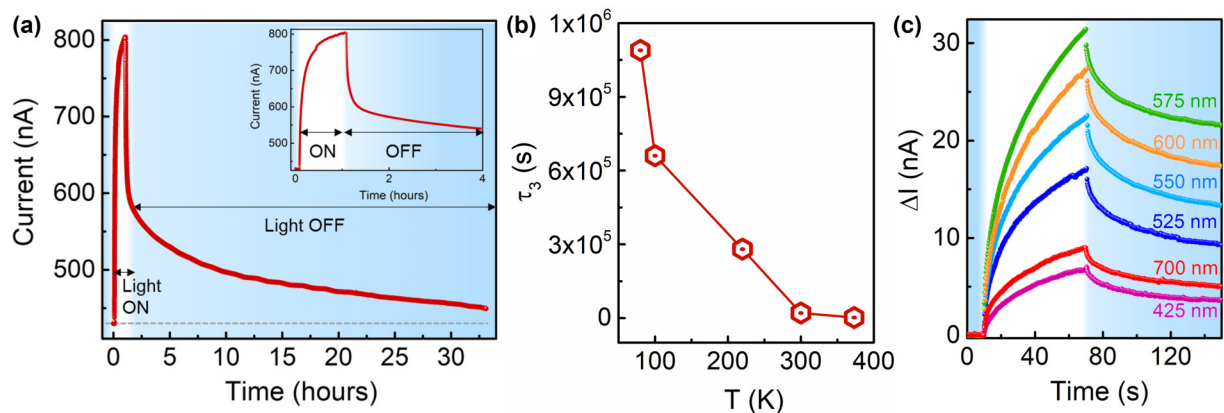


FIG. 3. (a) Photoresponse of ScN  $R_4$  showing the positive photoconductivity (PC) and the long persistence of PC even after the light is switched off. (b) The PC decay is fitted with three exponential functions that yield three time constants. The significantly large  $\tau_3$  (on the order of  $10^5$  s) is due to the spatial separation of the photogenerated carriers by the potential fluctuation. (c) Wavelength-dependent photoconductivity measurement reveals that the maximum change in photocurrent occurs for 575 nm (2.2 eV), corresponding to the direct band gap of ScN.

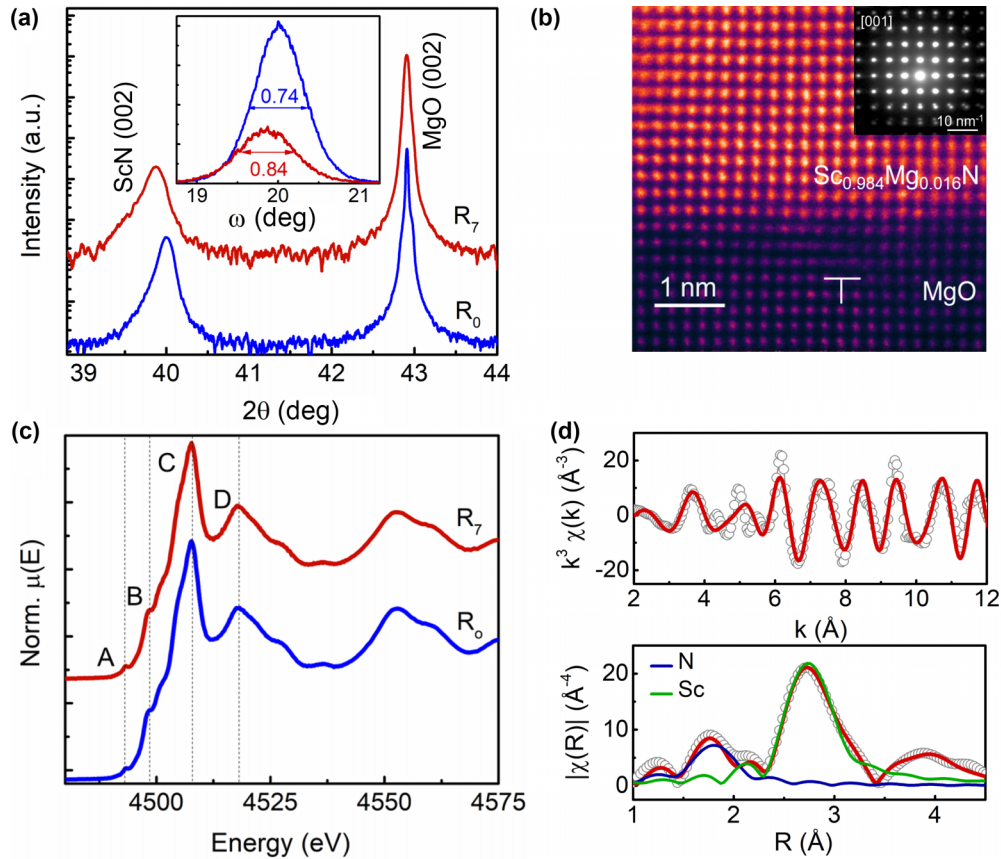


FIG. 4. (a) HRXRD for ScN  $R_0$  and  $R_7$  shows single crystallinity of both uncompensated and highly compensated ScN. The inset shows that the FWHM of the rocking curve of  $R_7$  is slightly higher than  $R_0$ . (b) Atomic-resolution STEM image presents the cubic epitaxial nature of the highly compensated  $R_7$  film. The inset shows the SAED pattern showing cubic Mg-compensated ScN grown on MgO. An edge dislocation is visible at the interface caused by the lattice mismatch. (c) Normalized Sc  $K$ -edge XANES spectra for  $R_0$  and  $R_7$  are similar. (d) Fourier transform moduli  $\chi(R)$  in  $R$  space and  $k^3$ -weighted  $|\chi(k)|$  for  $R_7$ .

hence the recombination becomes feasible. As a result,  $\tau_3$  decreases at higher temperatures (details in Appendix C). The wavelength-dependent photoconductivity measurement showed that the maximum change in current occurs for 575 nm illumination, which corresponds to the 2.2 eV direct band gap of the ScN [Fig. 3(c)]. The photocurrent and its persistence are lesser for photon energies lower than and above 2.2 eV, suggesting the maximum absorption of photons with energy corresponding to the direct band gap of ScN.

### C. Structural characterization across QAT

The striking feature of QAT in HDHCSs is that it arises in a single-crystalline semiconductor. There is absolutely no need for the structural disorder or phase segregation or compositional inhomogeneity that creates potential barriers like in conventional Anderson transition [8]. The high-resolution x-ray diffractogram (HRXRD) of an uncompensated ScN thin film on MgO ( $R_0$ ) [Fig. 4(a)] has two distinct peaks at  $39.9^\circ$  and  $42.9^\circ$  corresponding to (002) ScN and (002) MgO, respectively. The diffractogram of the highly compensated  $R_7$  plotted for comparison shows similar crystallinity with slight expansion in the lattice despite higher resistivity. The full width at half maximum (FWHM) of the  $\omega$ -rocking curve (shown in the inset) also does not significantly change,

indicating the retention of crystallinity during QAT. The high-resolution scanning transmission electron microscopic (HRSTEM) image shows the cubic epitaxial growth of highly compensated ScN ( $R_7$ ) on MgO [Fig. 4(b)]. The specific area electron diffraction (SAED) pattern in the inset of Fig. 4(b) also indicates the cubic epitaxial crystal growth.

The local geometric and electronic structure is further scrutinized with hard x-ray absorption spectroscopy (HXAS) studies carried out at the PETRA-64 synchrotron beamline [Fig. 4(c)]. The Sc  $K$ -edge x-ray absorption near-edge structure (XANES) spectra of  $R_0$  and  $R_7$  appear almost the same [Fig. 4(c)]. There are four peaks, labeled A, B, C, and D at 4492.9, 4498.3, 4507.7, and 4517.7 eV, respectively, and the peaks match well with the earlier reported XANES spectra of ScN [59]. The Fourier transform of  $|\chi(R)|$  in real space and  $k$  space for both  $R_0$  and  $R_7$  are fitted in ARTEMIS as in Fig. 4(d) (details in Appendix D). The position and intensity of every peak are almost the same for both  $R_0$  and  $R_7$ , suggesting no significant changes in the bonding or lattice distortion around the Sc absorber. The scattering paths are fitted with Sc as the scattering center.  $|\chi(R)|$  in real space is fitted up to 4 Å, covering two major shells [Fig. 4(d), bottom panel]. The Sc atom, being the central scatterer, is surrounded by a nitrogen shell at 1.76 Å and later

by Sc atoms at 2.7 Å. These two shells are clearly visible and well fitted for both  $R_0$  and  $R_7$ . Temperature-dependent HXAS measurement (Appendix D) also shows no structural changes.

#### IV. CONCLUSION

In conclusion, we report the quasiclassical Anderson transition (QAT) in single-crystalline compensated  $n$ -ScN thin films. The intentionally undoped ScN films are heavily  $n$  type with carrier concentration of  $1.2 \times 10^{21} \text{ cm}^{-3}$  and resistivity of  $1.8 \times 10^{-4} \Omega \text{ cm}$ , at room temperature. With Mg hole compensation, the resistivity increases by nine orders to  $1.5 \times 10^5 \Omega \text{ cm}$  at room temperature. Such a large change in resistivity is governed by the large-scale potential fluctuations arising from the inhomogeneous distribution of charged dopants, which localizes carriers into metallic droplets surrounded by potential barriers. The carrier transport in high-resistance ScN changes from hopping to percolation type on sufficient activation. The QAT in ScN is further evidenced by the anomalously low mobility that increases with increasing temperature, sign reversal of the Seebeck coefficient, and the persistence in photoconductivity. This work presents ScN as the first nitride material platform to explore exciting transport phenomena like QAT and opens up a gateway for interesting applications.

Data are available on request from the authors.

#### ACKNOWLEDGMENTS

D.R. and B.S. acknowledge the International Centre for Materials Science (ICMS) and Sheikh Saqr Laboratory (SSL) in JNCASR for support. B.S. acknowledges the Science and Engineering Research Board (SERB) of the Government of India, Start-Up Research Grant No. SRG/2019/000613, for financial support. D.R. thanks JNCASR for the fellowship. D.R. acknowledges SAMat research facilities. D.R. acknowledges Krishna Chand Maurya and Dr. Nidhi Pandey for the help in XAS measurement and analysis. A.I.K.P. and M.G. acknowledge the facilities of Sydney Microscopy and Microanalysis at The University of Sydney. Parts of this research were carried out at the PETRA III beamline P64. Beamtime was allocated for proposal I-20220131. Financial support by the DST provided within the framework of the India@DESY collaboration is gratefully acknowledged. D.R. and B.S. greatly acknowledge Prof. T. V. Ramakrishnan (Indian Institute of Science, Bangalore) for helpful comments and discussions.

D.R. and B.S. conceived this project. D.R. deposited the thin films and performed characterization and measurements. D.P.P. performed low-temperature electrical measurements. A.I.K.P. performed TEM sample preparation and M.G. performed TEM characterization. A.T. performed XAS measurements. D.R. and B.S. analyzed the results. All authors discussed and contributed to the preparation of the manuscript.

The authors declare no competing financial interest.

### APPENDIX A: CALCULATION OF VARIOUS PROPERTIES RELATED TO QAT AND PERCOLATIVE CHARGE TRANSPORT

#### 1. Critical electron concentration ( $n_c$ )

The critical electron concentration ( $n_c$ ) corresponding to the quasiclassical Anderson transition is given as [8]

$$n_c = \beta N^{2/3} / a \quad (13.1.1 \text{ in Ref. [8]}),$$

where  $\beta$  is the numerical coefficient  $\approx 0.5$  [8],  $a$  is the equivalent Bohr's radius of impurity, and  $N = 1/a^3$ .

For ScN,

$$a = \varepsilon \frac{m}{m^*} a_0 = (11.7) \frac{1}{0.39} (0.53 \text{ \AA}) = 1.59 \text{ nm}$$

and  $N = 2.5 \times 10^{20} \text{ cm}^{-3}$ . So,  $n_c = 1.25 \times 10^{20} \text{ cm}^{-3}$ .

#### 2. Minimum conductivity ( $\sigma_{\min}$ )

According to Mott, there exists a minimum metallic conductivity:

$$\sigma_{\min} = c_3 \frac{e^2}{\hbar} / N_M^{1/3},$$

where  $c_3 = 0.05$  and  $N_M$  is the minimum impurity concentration for a lightly doped semiconductor to become a heavily doped semiconductor. For ScN, with  $N_M = 2.5 \times 10^{20} \text{ cm}^{-3}$ ,  $\sigma_{\min}$  is calculated to be 76.67 S/cm.

However, it was later observed that the compensated semiconductors could have conductivity less than  $\sigma_{\min}$ . The metallic-to-insulator transition is not discontinuous but is sharp, with conductivity dropping steeply after  $\sigma_{\min}$  as  $\sigma(0) = 13\sigma_{\min} [(N/N_M) - 1]^{0.55}$  at 0 K. Though this observation is reported in Ref. [8] for Mott transition, we see it here for the quasiclassical Anderson transition.

#### 3. Radius of the carrier droplets ( $r_s$ )

The HDHCS obeys nonlinear screening. The radius of the droplets ( $r_s$ ) formed when carrier concentration is reduced to  $n$  is calculated as

$$r_s = \frac{N_t^{1/3}}{n^{1/3}} N_t = N_A + N_D.$$

The droplet radius increases from 2 to 350 nm as the electron concentration reduces from  $2 \times 10^{20}$  to  $1 \times 10^{17} \text{ cm}^{-3}$  as in Fig. 5.

#### 4. Amplitude of potential fluctuations ( $\gamma$ )

The amplitude of the fluctuation  $\gamma = \frac{e^2 N_t^{2/3}}{k n^{1/3}}$ , with  $k$  being the dielectric permittivity of the semiconductor. This amplitude equals the activation energy  $E_a$  for the carriers to reach the percolation level in two-dimensional potential relief. The percolation threshold  $\varepsilon_p$  depends on the dimensionality of space. In three-dimensional potential fluctuation (film thickness  $> r_s$ ), the  $\varepsilon_p$  is reduced to  $\varepsilon_p = -0.68\gamma$ . Thus, the activation energy  $E_a = 0.32\gamma$ . From this relation, the amplitude of the fluctuation for ScN is calculated, and its variation with carrier concentration is shown in Fig. 6.

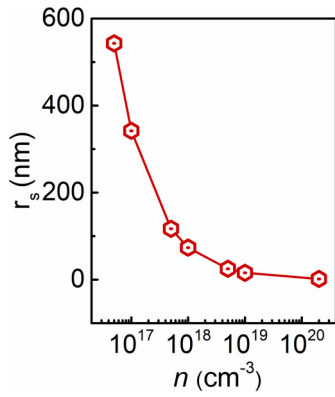


FIG. 5. The carrier droplet size increases as the carrier concentration decreases upon compensation.

### APPENDIX B: CARRIER TRANSPORT MECHANISM AT TEMPERATURES BELOW $T_c$

The carrier transport in HDHCSs has two regimes intersecting at critical temperature  $T_c$  as shown in Fig. 1(f). For temperatures above  $T_c$ , the carriers are activated to the percolation level and will percolate under the applied field. The carrier transport below  $T_c$  is also seen to have a temperature-dependent activation. The electrical transport can be described with a functional form  $\rho(T) = \rho_1 \exp(E_{a1}/kT) + \rho_2 \exp(E_{a2}/kT)^{1/2}$  in the entire temperature range with two distinct regimes intersecting at  $T_c$ . Physically, it means that in an HDHCS, where potential fluctuation leads to formation of metallic droplets surrounded by potential barriers, at high temperature ( $T > T_c$ ), conduction is dominated by the percolative charge transport with an activation energy ( $E_{a1}$ ), while at low temperatures ( $T < T_c$ ), as electrons do not have sufficient energy to overcome the potential barrier, they can only hop (tunnel at higher degree of compensation) from one droplet to another. This hopping of electrons also has an activation energy  $E_{a2}$ , which is smaller than the percolation activation energy.

Shklovskii and Efros analyzed the conduction at low temperatures carefully and suggested that a Coulomb gap could exist at low temperatures and the conductivity in this regime could be explained by replacing the localization radius in the original ES model with a length  $\hbar/\sqrt{|\mu|m}$  with  $\mu$  being the

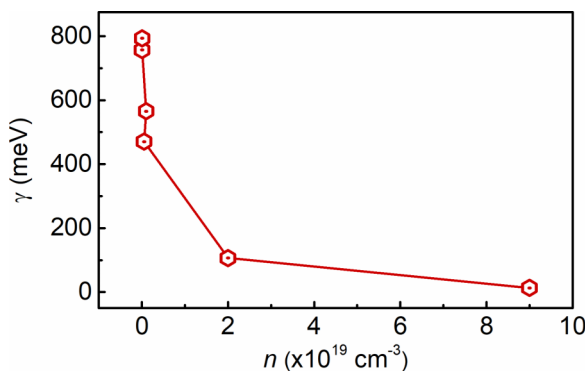


FIG. 6. The amplitude of potential fluctuation ( $\gamma$ ) increases as the carrier concentration decreases upon compensation.

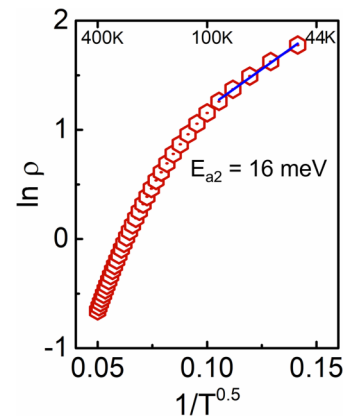


FIG. 7. The  $\ln \rho$  vs  $(1/T)^{1/2}$  plot indicating an ES-VRH at low temperatures for sample  $R_2$  with an activation energy of 16 meV.

barrier height [8]. The Coulomb-gap-driven ES variable range hopping has a function from  $\rho(T) = \rho_0 \exp(E_a/kT)^{1/2}$ .

The low-temperature transport of  $R_2$  film presented in Fig. 1(f) is fitted with an ES-VRH function and revealed a hopping barrier energy of 16 meV (Fig. 7). Similar to the  $R_2$  film, the low-temperature resistivity vs temperature below the  $T_c$  region of all other films is also fitted, showing good fitting. Thus, the low-temperature electron transport could be ES variable range hopping with a certain activation energy based on the degree of compensation.

### APPENDIX C: PHOTOCURRENT MEASUREMENT

The persistence in the photocurrent is an indication of the existence of potential fluctuation. Indium (In) contacts are pressed onto the ScN films to achieve Ohmic contact. Keithley 2450 is used to apply a constant voltage bias and measure current as a function of time. The  $I$ - $V$  of ScN with In contact is linear even for highly compensated ScN  $R_6$  and  $R_7$ , as in Fig. 8. Since In makes an Ohmic contact with low carrier highly resistive ScN films, it obviously forms Ohmic contact with all other lower resistive films as evidenced by the experiment. The sample is kept in the dark to equilibrate the dark current. A constant minimum bias is applied to measure

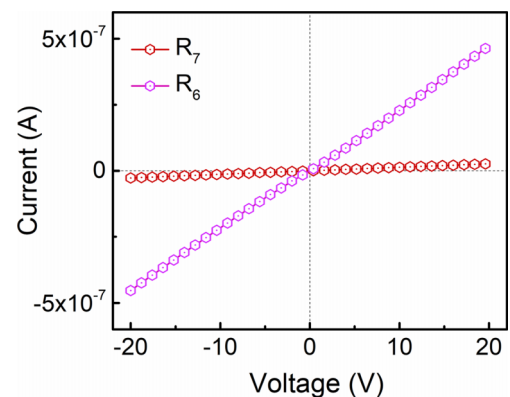


FIG. 8. The  $I$ - $V$  sweep of  $R_6$  and  $R_7$  with indium contact yields a straight line, suggesting the Ohmic contact formation at the In/ScN interface.

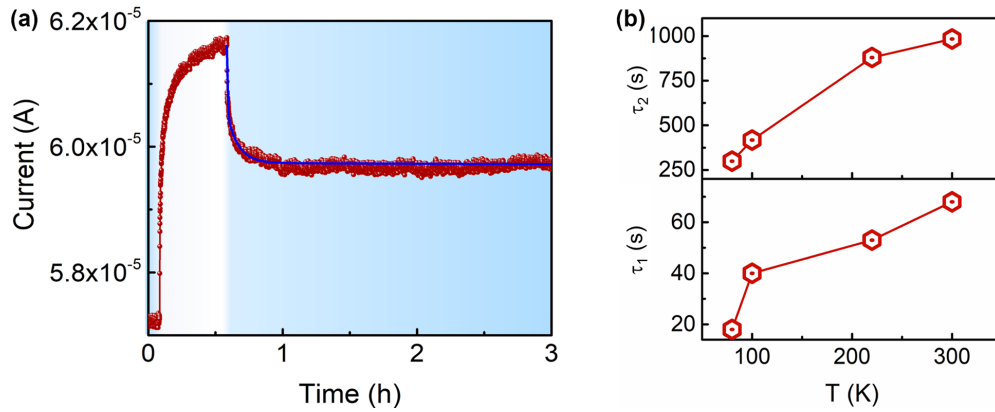


FIG. 9. (a) Three exponential fittings of the experimentally obtained photocurrent decay for Mg-compensated ScN film at 100 K. (b) Time constants  $\tau_1$  and  $\tau_2$  increase with increasing temperature.

the current and collect the photogenerated carriers at the electrodes. The bias voltages were varied from 0.1 to 30 V based on the resistivity of the sample to get at least a few hundred nanoamperes of current that can be measured precisely by the instrument. White light from the Xe arc lamp (250–2500 nm) is incident on the sample. The current in the compensated ScN increases on illumination, exhibiting positive photoconductivity.

Generally, the PPC decay is fitted with the stretched exponential function. However, in this case, the sharp initial decay prohibits using stretched exponential decay. Hence, the photocurrent decay is fitted with three exponential functions with the following equation:

$$I = I_0 + Ae^{-\frac{(t-t_0)}{\tau_1}} + Be^{-\frac{(t-t_0)}{\tau_2}} + Ce^{-\frac{(t-t_0)}{\tau_3}}.$$

The above equation fits well to the obtained experimental data in the 100–400 K temperature range [the representative fit for 100 K is shown in Fig. 9(a)]. The first two time constants,  $\tau_1$  and  $\tau_2$ , are in the range of tens and hundreds of seconds and increase at higher temperatures [Fig. 9(b)]. This effect is attributed to the electron redistribution at the percolation sites, as in Ref. [60]. The third time constant  $\tau_3$  is in the range of  $10^5$  s and is responsible for the long persistence of photocurrent [Fig. 3(b)].  $\tau_3$  decreases at higher temperatures as the photogenerated carriers gain energy to overcome the fluctuation barriers and recombine. In the range 100–400 K, the nature of photoconductivity remains positive. However, the amplitude of percentage change in photocurrent is higher at lower temperatures and so is the persistence. This can be attributed to the higher dark current at a higher temperature compared to the lower temperatures below  $T_c$ .

Wavelength-dependent photoconductivity was measured using the NKT supercontinuum laser with a SuperK VARIA visible-band monochromator. The laser power at every wavelength is set so that the incident intensity of all the wavelengths is 1.5 mW. For the wavelength-dependent measurements, since we are interested in the amount of photocurrent ( $\Delta I$ ) increase with respect to the wavelength of the incident light, we illuminate the sample for a few seconds and wait until the photocurrent decays significantly to a lower level for the subsequent measurements. Since the films  $R_6$  and  $R_7$  have very long persistence as in Fig. S6(b) [12], we use

samples  $R_4$  (and  $R_2$  presented in SM Sec. III) with relatively lower persistence to study the wavelength-dependent photoreponse and the photocurrent persistence.

#### APPENDIX D: LOCAL STRUCTURE ANALYSIS USING X-RAY ABSORPTION SPECTROSCOPY

The structure is analyzed with x-ray absorption spectroscopy (XAS) in the PETRA-64 beamline in reflection mode. The XANES and extended x-ray-absorption fine structure (EXAFS) data for the Sc  $K$  edge are collected from 4292 to 5150 eV. The background is subtracted, and pre- and post-edge corrections followed by normalization are performed using ATHENA software. The spectrum looks the same for uncompensated and highly compensated ScN  $R_0$  and  $R_7$  [Fig. 4(c)]. There are four peaks, labeled A, B, C, and D at 4492.9, 4498.3, 4507.7, and 4517.7 eV, respectively. The  $K$  edge has shifted to the higher energy of 4503.7 eV compared to that of metallic Sc (4492 eV), indicating the nitridation. There are two pre-edges, one at 4492.9 eV and the other at 4498.3 eV, designated as A and B. Peak A intensity is very small and could arise due to noncentrosymmetric atomic environments. Peak B occurs due to the electric quadrupole transition of an electron from Sc  $1s$  to  $3d$  mixed with N  $2p$  to give some overlap of states. The intense peak C is attributed to the allowed  $1s$ -to- $4p$  dipole transition. Further transition to higher hybridized states results in peak D. The peaks were reported earlier by Choudary *et al.* [59].

The Fourier transform of  $|\chi(R)|$  in real space and  $k$  space is calculated from the normalized spectra in ARTEMIS [Figs. 10(a) and 10(b)]. The transformation and further fitting of the NaCl structured ScN with  $a = 4.509$  Å is done using ARTEMIS. The scattering paths are fitted with Sc as the scattering center.  $|\chi(R)|$  in real space is fitted up to 4 Å, covering two major shells [Fig. 4(d)]. The Sc atom, being the central scatterer, is surrounded by a nitrogen shell at 1.76 Å and later by Sc atoms at 2.7 Å. These two shells are clearly visible and well fitted for both  $R_0$  and  $R_7$ . The intensity of the features is higher for  $R_7$  until the first N shell, and then the  $R_0$  is higher. Also, the peak corresponding to the N shell is slightly shifted to the right, indicating the expansion of the lattice due to the Mg substitution. The effect of Mg substitution is seen only in the first shell. At larger distances from the Sc

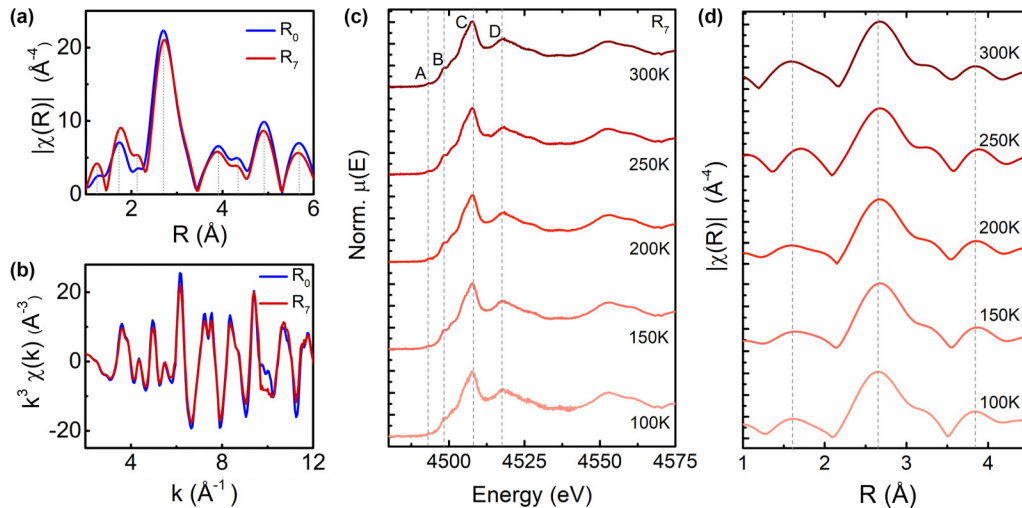


FIG. 10. Comparison of Fourier transform moduli  $\chi(R)$  in (a)  $R$  space and (b)  $k^3$ -weighted  $|\chi(R)|$  for  $R_0$  and  $R_7$  indicates no significant changes in the local environment of Sc upon high compensation. (c) Temperature-dependent XANES of  $R_7$  indicates no structural change in the 100–300 K range. (d) Temperature-dependent Fourier transform moduli  $\chi(R)$  in  $R$  space of  $R_7$  indicates no significant change in bond lengths around the Sc scatterer in the 100–300 K range.

scatter, the lattice is not significantly disturbed. The  $\chi(k) \times k^3$  is also fitted well in the range of 2 to 12  $\text{\AA}^{-1}$  [Fig. 4(d)]. Thus, apart from the slight expansions, the crystallinity is preserved during QAT in ScN.

Temperature-dependent XANES of highly compensated ScN  $R_7$  is shown in Fig. 10(c). The spectra remain the same from 100 to 300 K across the QAT. The Fourier transform

of  $|\chi(R)|$  in real space in the studied temperature range is also similar [Fig. 10(d)]. The activation in the conductivity of HDHCS above  $T_c$  is not accompanied by any structural changes. The transition from insulating to metal-like conduction occurs due to the onset of percolative transport on thermal activation.

- 
- [1] P. W. Anderson, Absence of diffusion in certain random lattices, *Phys. Rev.* **109**, 1492 (1958).
- [2] N. F. Mott and J. H. Davies, Metal-insulator transition in doped semiconductors, *Philos. Mag. B* **42**, 845 (1980).
- [3] A. A. Chabanov, M. Stoytchev, and A. Z. Genack, Statistical signatures of photon localization, *Nature (London)* **404**, 850 (2000).
- [4] J. Mendoza and G. Chen, Anderson localization of thermal phonons leads to a thermal conductivity maximum, *Nano Lett.* **16**, 7616 (2016).
- [5] S. Chakravarty and A. Schmid, Weak localization: The quasi-classical theory of electrons in a random potential, *Phys. Rep.* **140**, 193 (1986).
- [6] J. Wang, W. Powers, Z. Zhang, M. Smith, B. J. McIntosh, S. K. Bac, L. Riney, M. Zhukovskiy, T. Orlova, L. P. Rokhinson, Y. T. Hsu, X. Liu, and B. A. Assaf, Observation of coexisting weak localization and superconducting fluctuations in strained  $\text{Sn}_{1-x}\text{In}_x\text{Te}$  thin films, *Nano Lett.* **22**, 792 (2022).
- [7] P. A. Lee and T. V. Ramakrishnan, Disordered electronic systems, *Rev. Mod. Phys.* **57**, 287 (1985).
- [8] B. I. Shklovskii and A. L. Efros, *Electronic Properties of Doped Semiconductors*, 1st ed. (Springer, Berlin, 1984).
- [9] B. G. Arnaudov, D. S. Domanevskii, and I. Y. Yanchev, Hopping conductivity in heavily doped strongly compensated GaAs, *Phys. Status Solidi* **91**, 311 (1979).
- [10] D. D. Nolte, Semi-insulating semiconductor heterostructures: Optoelectronic properties and applications, *J. Appl. Phys.* **85**, 6259 (1999).
- [11] V. F. Mitin, Preparation and properties of heavily doped and strongly compensated Ge films on GaAs, *J. Appl. Phys.* **107**, 033720 (2010).
- [12] See Supplemental Material at <http://link.aps.org/supplemental/10.1103/PhysRevB.109.155307> for the structural, compositional, and optical characterization, and additional data for photocurrent measurements and low-temperature electrical measurements.
- [13] V. F. Mitin, Heavily doped and fully compensated Ge single-crystalline films on GaAs, *Appl. Phys. Lett.* **92**, 202111 (2008).
- [14] T. F. Rosenbaum, R. F. Milligan, M. A. Paalanen, G. A. Thomas, R. N. Bhatt, and W. Lin, Metal-insulator transition in a doped semiconductor, *Phys. Rev. B* **27**, 7509 (1983).
- [15] V. Kažukauskas, J. Storasta, and J. V. Vaitkus, Interaction of deep levels and potential fluctuations in scattering and recombination phenomena in semi-insulating GaAs, *J. Appl. Phys.* **80**, 2269 (1996).
- [16] E. Oh, H. Park, and Y. Park, Influence of potential fluctuation on optical and electrical properties in GaN, *Appl. Phys. Lett.* **72**, 1848 (1998).

- [17] S. Siebentritt, N. Papathanasiou, and M. C. Lux-Steiner, Potential fluctuations in compensated chalcopyrites, *Phys. B Condens. Matter* **376**, 831 (2006).
- [18] P. Das, B. Biswas, K. C. Maurya, M. Garbrecht, and B. Saha, Refractory plasmonic hafnium nitride and zirconium nitride thin films as alternatives to silver for solar mirror applications, *ACS Appl. Mater. Interfaces* **14**, 46708 (2022).
- [19] O. Elmazria, M. B. Assouar, P. Renard, and P. Alnot, Electrical properties of piezoelectric aluminium nitride films deposited by reactive DC magnetron sputtering, *Phys. Status Solidi Appl. Res.* **196**, 416 (2003).
- [20] J. ed. Piprek, *Nitride Semiconductor Devices Principles and Simulation* (Wiley, New York, 2007).
- [21] S. Nakamura, Current status of GaN-based solid state lighting, *MRS Bull.* **34**, 101 (2009).
- [22] B. Saha, A. Shakouri, and T. D. Sands, Rocksalt nitride metal/semiconductor superlattices: A new class of artificially structured materials, *Appl. Phys. Rev.* **5**, 021101 (2018).
- [23] B. Biswas and B. Saha, Development of semiconducting ScN, *Phys. Rev. Mater.* **3**, 020301 (2019).
- [24] H. Obloh, K. H. Bachem, U. Kaufmann, M. Kunzer, M. Maier, A. Ramakrishnan, and P. Schlotter, Self-compensation in Mg doped p-type GaN grown by MOCVD, *J. Cryst. Growth* **195**, 270 (1998).
- [25] Z. Gu, J. H. Edgar, J. Pomeroy, M. Kuball, and D. W. Coffey, Crystal growth and properties of scandium nitride, *J. Mater. Sci. Mater. Electron.* **15**, 555 (2004).
- [26] J. H. Edgar, T. Bohnen, and P. R. Hageman, HVPE of scandium nitride on 6H-SiC(0 0 1), *J. Cryst. Growth* **310**, 1075 (2008).
- [27] Y. Oshima, E. G. Villora, and K. Shimamura, Hydride vapor phase epitaxy and characterization of high-quality ScN epilayers, *J. Appl. Phys.* **115**, 153508 (2014).
- [28] J. P. Dismukes, W. M. Yim, and V. S. Ban, Epitaxial growth and properties of semiconducting ScN, *J. Cryst. Growth* **13**, 365 (1972).
- [29] H. A. Al-Britthen, A. R. Smith, and D. Gall, Surface and bulk electronic structure of ScN(001) investigated by scanning tunneling microscopy/spectroscopy and optical absorption spectroscopy, *Phys. Rev. B* **70**, 045303 (2004).
- [30] B. Saha, G. Naik, V. P. Drachev, A. Boltasseva, E. E. Marinero, and T. D. Sands, Electronic and optical properties of ScN and (Sc,Mn)N thin films deposited by reactive DC-magnetron sputtering, *J. Appl. Phys.* **114**, 063519 (2013).
- [31] P. V. Burmistrova, J. Maassen, T. Favaloro, B. Saha, S. Salamat, Y. Rui Koh, M. S. Lundstrom, A. Shakouri, and T. D. Sands, Thermoelectric properties of epitaxial ScN films deposited by reactive magnetron sputtering onto MgO(001) substrates, *J. Appl. Phys.* **113**, 153704 (2013).
- [32] D. Rao, B. Biswas, E. Flores, A. Chatterjee, M. Garbrecht, Y. R. Koh, V. Bhatia, A. I. K. Pillai, P. E. Hopkins, M. Martin-Gonzalez, and B. Saha, High mobility and high thermoelectric power factor in epitaxial ScN thin films deposited with plasma-assisted molecular beam epitaxy, *Appl. Phys. Lett.* **116**, 152103 (2020).
- [33] S. Kerdsonpanya, N. Van Nong, N. Pryds, A. Žukauskaite, J. Jensen, J. Birch, J. Lu, L. Hultman, G. Wingqvist, and P. Eklund, Anomalously high thermoelectric power factor in epitaxial ScN thin films, *Appl. Phys. Lett.* **99**, 232113 (2011).
- [34] A. Le Febvrier, N. Tureson, N. Stölkerich, G. Greczynski, and P. Eklund, Effect of impurities on morphology, growth mode, and thermoelectric properties of (1 1 1) and (0 0 1) epitaxial-like ScN films, *J. Phys. D. Appl. Phys.* **52**, 035302 (2019).
- [35] D. Rao, O. Chowdhury, A. I. K. Pillai, G. K. Pradhan, S. Sahoo, J. P. Feser, M. Garbrecht, and B. Saha, Multifunctional irradiation-induced defects for enhancing thermoelectric properties of scandium nitride thin films, *ACS Appl. Energy Mater.* **5**, 6847 (2022).
- [36] M. A. Moram, Y. Zhang, M. J. Kappers, Z. H. Barber, and C. J. Humphreys, Dislocation reduction in gallium nitride films using scandium nitride interlayers, *Appl. Phys. Lett.* **91**, 152101 (2007).
- [37] L. Lupina, M. H. Zoellner, T. Niermann, B. Dietrich, G. Capellini, S. B. Thapa, M. Haebleren, M. Lehmann, P. Storck, and T. Schroeder, Zero lattice mismatch and twin-free single crystalline ScN buffer layers for GaN growth on silicon, *Appl. Phys. Lett.* **107**, 201907 (2015).
- [38] K. C. Maurya, D. Rao, S. Acharya, P. Rao, A. I. K. Pillai, S. K. Selvaraja, M. Garbrecht, and B. Saha, Polar semiconducting scandium nitride as an infrared plasmon and phonon-polaritonic material, *Nano Lett.* **22**, 5182 (2022).
- [39] J. Casamento, J. Wright, R. Chaudhuri, H. Xing, and D. Jena, Molecular beam epitaxial growth of scandium nitride on hexagonal SiC, GaN, and AlN, *Appl. Phys. Lett.* **115**, 172101 (2019).
- [40] A. R. Smith, H. A. H. Al-Britthen, D. C. Ingram, and D. Gall, Molecular beam epitaxy control of the structural, optical, and electronic properties of ScN(001), *J. Appl. Phys.* **90**, 1809 (2001).
- [41] D. Rao, B. Biswas, S. Acharya, V. Bhatia, A. I. K. Pillai, M. Garbrecht, and B. Saha, Effects of adatom mobility and Ehrlich-Schwoebel barrier on heteroepitaxial growth of scandium nitride (ScN) thin films, *Appl. Phys. Lett.* **117**, 212101 (2020).
- [42] J. More-Chevalier, S. Cichoń, L. Horák, J. Bulř, P. Hubík, Z. Gedeonová, L. Fekete, M. Poupon, and J. Lančok, Correlation between crystallization and oxidation process of ScN films exposed to air, *Appl. Surf. Sci.* **515**, 145968 (2020).
- [43] S. W. King, R. F. Davis, and R. J. Nemanich, Gas source molecular beam epitaxy of scandium nitride on silicon carbide and gallium nitride surfaces, *J. Vac. Sci. Technol. A Vacuum, Surfaces, Film.* **32**, 061504 (2014).
- [44] T. Ohgaki, K. Watanabe, Y. Adachi, I. Sakaguchi, S. Hishita, N. Ohashi, and H. Haneda, Electrical properties of scandium nitride epitaxial films grown on (100) magnesium oxide substrates by molecular beam epitaxy, *J. Appl. Phys.* **114**, 093704 (2013).
- [45] D. Rao, A. I. K. Pillai, M. Garbrecht, and B. Saha, Scandium nitride as a gateway III-nitride semiconductor for both excitatory and inhibitory optoelectronic artificial synaptic devices, *Adv. Electron. Mater.* **9**, 2200975 (2023).
- [46] B. Saha, M. Garbrecht, J. A. Perez-Taborda, M. H. Fawey, Y. R. Koh, A. Shakouri, M. Martin-Gonzalez, L. Hultman, and T. D. Sands, Compensation of native donor doping in ScN: Carrier concentration control and p-type ScN, *Appl. Phys. Lett.* **110**, 252104 (2017).
- [47] S. Rudra, D. Rao, S. Poncé, and B. Saha, Reversal of band-ordering leads to high hole mobility in strained p-type scandium nitride, *Nano Lett.* **23**, 8211 (2023).

- [48] S. Nayak, M. Baral, M. Gupta, J. Singh, M. Garbrecht, T. Ganguli, S. M. Shivaprasad, and B. Saha, Rigid-band electronic structure of scandium nitride across the n-type to p-type carrier transition regime, *Phys. Rev. B* **99**, 161117(R) (2019).
- [49] J. More-Chevalier, L. Horák, S. Cichon, P. Hruška, J. Cížek, M. O. Liedke, M. Butterling, A. Wagner, J. Bulír, P. Hubík, Z. Gedeonová, and J. Lancok, Positron structural analysis of ScN films deposited on MgO substrate, *Acta Phys. Pol. A* **137**, 209 (2020).
- [50] Y. Kumagai, N. Tsunoda, and F. Oba, Point defects and p-type doping in ScN from first principles, *Phys. Rev. Appl.* **9**, 034019 (2018).
- [51] I.-H. Lee, J. J. Lee, P. Kung, F. J. Sanchez, and M. Razeghi, Band-gap narrowing and potential fluctuation in Si-doped GaN, *Appl. Phys. Lett.* **74**, 102 (1999).
- [52] M. S. Haseman, B. A. Noesges, S. Shields, J. S. Cetnar, A. N. Reed, H. A. Al-Atabi, J. H. Edgar, and L. J. Brillson, Cathodoluminescence and x-ray photoelectron spectroscopy of ScN: Dopant, defects, and band structure, *APL Mater.* **8**, 081103 (2020).
- [53] K. Lal, A. K. Meikap, S. K. Chattopadhyay, S. K. Chatterjee, M. Ghosh, K. Baba, and R. Hatada, Electrical resistivity of titanium nitride thin films prepared by ion beam-assisted deposition, *Phys. B Condens. Matter* **307**, 150 (2001).
- [54] T. F. Rosenbaum, K. Andres, G. A. Thomas, and R. N. Bhatt, Sharp metal-insulator transition in a random solid, *Phys. Rev. Lett.* **45**, 1723 (1980).
- [55] A. Shik, Hall effect and electron mobility in inhomogeneous semiconductors, *JETP Lett.* **20**, 5 (1974).
- [56] V. G. Karpov, A. Y. Shik, and B. I. Shklovskii, Theory of the Hall effect in randomly inhomogeneous semiconductors, *Sov. Physics. Semicond.* **16**, 901 (1982).
- [57] A. V. Shik, Photoconductivity of randomly-inhomogeneous semiconductors, *Sov. Phys.-JETP* **41**, 932 (1975).
- [58] H. X. Jiang and J. Y. Lin, Persistent photoconductivity and related critical phenomena in  $Zn_{0.3}Cd_{0.7}Se$ , *Phys. Rev. B* **40**, 10025 (1989).
- [59] S. Chowdhury, R. Gupta, P. Rajput, A. Tayal, D. Rao, R. Sekhar, S. Prakash, R. Rajagopalan, S. N. Jha, B. Saha, and M. Gupta, Detailed study of reactively sputtered ScN thin films at room temperature, *Materialia* **22**, 101375 (2022).
- [60] H. X. Jiang and J. Y. Lin, Percolation transition of persistent photoconductivity in II-VI mixed crystals, *Phys. Rev. Lett.* **64**, 2547 (1990).